



# Soft pinning of liquid domains on topographical hemispherical caps



Luigi Feriani<sup>a,b</sup>, Luigi Cristofolini<sup>a</sup>, Pietro Cicuta<sup>b,\*</sup>

<sup>a</sup> Dipartimento di Fisica e Scienze della Terra “Macedonio Melloni”, Università di Parma, Viale Usberti 7/A, 43124 Parma, Italy

<sup>b</sup> Cavendish Laboratory, University of Cambridge, JJ Thomson Avenue, CB3 0HE Cambridge, UK

## ARTICLE INFO

### Article history:

Available online 7 August 2014

### Keywords:

Membrane domains  
Phase separation  
Topographical pinning  
Membrane curvature

## ABSTRACT

The role of lipid composition as a regulator or mediator of processes that take place in biological membranes is a very topical question, and important insights can be gained by studying in vitro model lipid mixture systems. A particular question is the coupling of local curvature to the local phases in membranes of mixed composition. Working with an experimental system of giant unilamellar vesicles of ternary composition, the curvature is imposed by approaching the membrane to a topographically (on the micron scale) patterned surface. Performing experiments, we show that domains of the more disordered phase localise preferentially to regions of higher curvature. We characterise and discuss the strength of this “caging” behaviour. In future, the setup we discuss here could prove useful as a platform to localise domains rich in membrane proteins, or to promote the onset of biochemical processes at specific locations. Finally, we note that the methods developed here could have also applications in bio-sensing, as a similar but metal coated topography can sustain plasmonic resonances.

Crown Copyright © 2014 Published by Elsevier Ireland Ltd. All rights reserved.

## 1. Introduction

Artificial lipid bilayers are interesting systems from many different perspectives: their self-assembling nature makes them relatively easy to manipulate in ambient conditions, and they are a useful 2D model system to study new physics questions and to trial designs of hierarchical complexity. They are also useful model systems to understand biological processes, as their physical-chemical properties underpin various functional aspects of biological membranes, which in turn are a fundamental component of cells. Of particular interest to ourselves and others, multicomponent lipid membranes are the simplest model to study liquid–liquid phase separation, possibly linked to the concept of lipid “rafts” which have been proposed as an important aspect of lipid–protein interactions in the plasma membrane of cells, and linked to adhesion, endocytosis, protein complexation, apoptosis, and lipid regulation (Simons and Ikonen, 1997; Edidin, 2001; Veatch and Keller, 2002).

This paper focuses on the influence of curvature on the lateral organisation of liquid–liquid phase separated lipid bilayers. This particular aspect is very interesting for biology, as it could shed some light on the sensitivity to the curvature shown by some membrane proteins (Parthasarathy et al., 2006; Mouritsen, 2011), and more generally to the coupling of curvature to lipid composition

(Sorre et al., 2009; Kamal et al., 2009; Tian and Baumgart, 2009). In turn, protein localisation is linked to complex processes, such as the growth of actin filaments (Gallop and Walrant, 2013), that seem to be influenced by curvature.

Finally, understanding how phase separated bilayers laterally organise in presence of locally induced curvature may lead us to harness this effect for practical purposes such as bio-sensing: for example, localising particular membrane components or membrane bound species to species a pattern on the nano- or micro-scale could make a powerful combination with plasmonic resonance probes (Christensen and Stamou, 2010).

A brief literature review and background information are provided in Section 2, then the experimental methods, which cover the crafting of the microstructured surface, the preparation of lipid bilayers, and the imaging methods are given in Section 3. The analysis of domain localisation is reported in Section 4. The main result shown here is the preferential localisation of liquid disordered domains onto topographical bumps.

## 2. Background

### 2.1. Liquid–liquid phase separation

Biological membranes are composed of thousands of lipid species, well regulated in the various subcellular organelles (van Meer et al., 2008). The protein concentration is also high (by weight and area fraction, but not as a molar fraction). Despite this

\* Corresponding author. Tel.: +44 1223 337 462; fax: +44 1223 337 000.  
E-mail address: [pc245@cam.ac.uk](mailto:pc245@cam.ac.uk) (P. Cicuta).

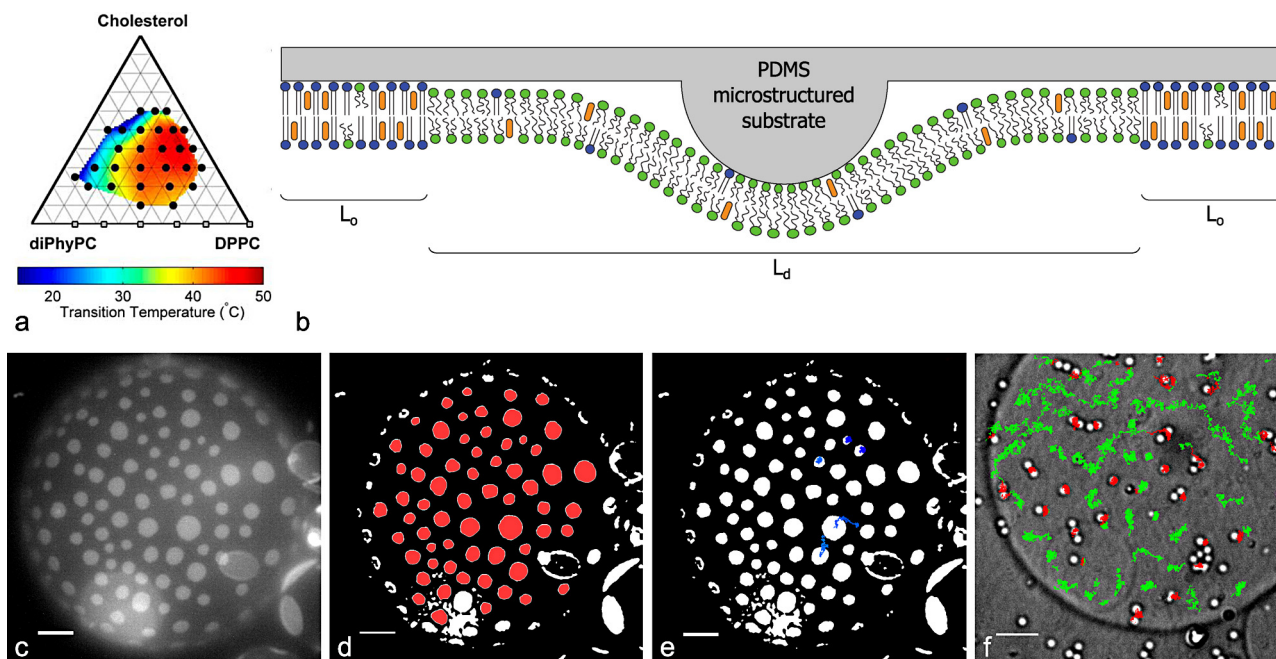


**Fig. 1.** (a) The phase diagram of a system very close to the one investigated here has been published in Veatch et al. (2006), and shows an extended (and temperature dependent) region of coexistence between a liquid disordered and a liquid ordered phase; (b) schematic of the experimental condition in the experiments carried out in this work, where the top of a Giant Unilamellar Vesicle is brought close to a patterned substrate, so that the lipid membrane bilayer is pressed against the hemispherical “bump” topography. (c,d,e,f) Optical microscopy images of domains and bumps, illustrating the steps taken in image analysis: (c) is a frame, as obtained by epifluorescence; (d) is the result of filtering and thresholding, and the shaded domains are the ones that survive the rejection criteria, and are used in later analysis; (e) shows as an example five tracks, superposed to the filtered and thresholded first frame of the time lapse; (f) all the “on-bump” domain tracks are plotted in red, the “off-bump” tracks in green. The tracks are superposed to a bright field image of the vesicle in contact with the patterned substrate: the bright spots are the bumps, and the dark circle is the outline of the vesicle. (For interpretation of the references to colour in this figure legend, the reader is referred to the web version of the article.)

richness in composition, membranes exhibit similar thermodynamical behaviour to much simpler systems, such as ternary mixtures made of a saturated lipid, an unsaturated one and a sterol (Veatch et al., 2008; Honerkamp-Smith et al., 2008). What is observed in these mixtures is a region (bounded in composition, and temperature) of phase coexistence between two liquid regions, one enriched in the saturated lipid and cholesterol, the other enriched in the unsaturated lipid (Veatch and Keller, 2002; Veatch et al., 2008). These phases are named liquid-ordered ( $L_o$ ) and liquid-disordered ( $L_d$ ) respectively, see Fig. 1(a). A wide variety of ternary lipid mixtures containing a high melting temperature ( $T_m$ ) lipid (usually with saturated acyl tails), a low  $T_m$  one (usually unsaturated) and a sterol have been shown to exhibit coexistence of liquid phases (Veatch and Keller, 2005). These liquid phases have been observed both in Giant Unilamellar Vesicles (GUVs) and in supported bilayers.

In model systems, phase separation can be induced for example by cooling a system prepared at close to its critical composition; then, coexisting phases are formed by spinodal decomposition, or by nucleation and growth (Stanich et al., 2013). In some experiments, this separation process proceeds to completion, i.e., domains coalesce until the system is made of only two spatially distinct regions. In other experiments, and particularly in closed systems such as vesicles, where constraining the enclosed volume imposes strong constraints to the allowed overall vesicle shape, meso-scopic domains are seen to coalesce very slowly, or even to remain stable over time Idema et al. (2010). It is not clear if these intermediate phases are metastable states, or equilibrium states of the system. In either case, domains always exist in the system for a long time (even when domain coalescence is not hindered, micron-sized domains exist for tens of minutes during coarsening).

Both phases are liquid, and characterised by fast lateral diffusion, high rotational freedom and short range order, but they

present some important differences, in both composition and physical properties (Hirst et al., 2011). The  $L_o$  region of the membrane is around 1 nm thicker (characterised with AFM measurements (Burns et al., 2005; Lawrence et al., 2003)) and has higher bending modulus and viscosity; the differences between phases depend on the point of the diagram phase, vanishing as the critical point is approached (Connell et al., 2013; Yoon et al., 2010; Cicuta et al., 2007). It is important to note that the lipid domains have been shown to be in registry between the two leaflets of the bilayer (Korlach and Schwille, 1999; Marrink et al., 2007; Collins and Keller, 2008; Collins, 2008).

## 2.2. Physical properties

Lipid domain morphology is determined, in the plane of the membrane, by the line tension  $\sigma$  (the two dimensional analogue of surface tension). This tends to minimise the energy cost of the phase boundaries by maintaining circular lipid domains. Line tension has been characterised by flicker spectroscopy of fluorescently labelled domains in ternary GUVs (Honerkamp-Smith et al., 2008), and by AFM on supported lipid bilayers (Connell et al., 2013). The line tension decreases linearly as a function of the temperature difference to the critical temperature. In the work presented here the line tension is between 0.4 and 1.2 pN (Honerkamp-Smith et al., 2008).

The motility of domains is controlled by their size, and by the viscosity of the surrounding membrane. When the surrounding has high viscosity (typically, when it is in the  $L_o$  phase), then membrane viscosity can be extracted from the diffusivity of lipid domains in a Brownian regime (Cicuta et al., 2007; Petrov and Schwille, 2008). In the conditions of this work, the  $L_o$  phase has a viscosity of the order of  $10^{-7}$ Ns/m (Cicuta et al., 2007).

If out-of-plane deformation is at play, then a third physical quantity is relevant, the bending modulus  $\kappa$ . In the conditions of this work, the  $L_d$  and  $L_o$  phases have bending moduli of around 25–45, and 40–100  $k_B T$  respectively (Yoon et al., 2010). The range in  $\kappa$ , and  $\sigma$  above, comes from the fact that we do not know the precise distance to the critical temperature: it can differ by a few degrees for different vesicles in the same batch, and we estimate the experiments to be in the range between 5 and 10 degrees from critical.

### 2.3. Shape-dependent energy

The shape of a lipid vesicle can be calculated by minimising the total energy functional, under appropriate constraints. Area is always assumed fixed (at constant temperature and constant number of molecules), whereas the internal volume might or not be physically constrained depending if the system is permeable to water in the timescale of interest (membranes have some permeability to water (Graziani and Livne, 1972), so a difference in osmolarity will cause a net water flow through the membrane until the osmotic equilibrium is reached or the GUV bursts (Borsali and Pecora, 2008)).

The free energy for a liquid–liquid phase-separated lipid vesicle has various local and global contributions: at a minimum, one needs to consider the resistance to bending, lateral tension, and line tension of the phase boundaries (Baumgart et al., 2003). The interplay between these contributions causes the phase-separated vesicles to show a wide variety of behaviours and shapes under different conditions; for axi-symmetric shapes, it is possible to study these functionals analytically (Jülicher and Lipowsky, 1996; Lipowsky and Dimova, 2003; Baumgart et al., 2003; Semrau et al., 2009).

Following (Jülicher and Lipowsky, 1996), for a vesicle that presents two liquid phases  $\alpha$  and  $\beta$ , the total energy can be written as

$$F = F_m + F_b + F_G, \quad (1)$$

where  $F_m$  and  $F_G$  are, respectively, the normal and Gaussian bending energy, while

$$F_m = A^{(\alpha)}f^{(\alpha)} + A^{(\beta)}f^{(\beta)} + F_l \quad (2)$$

denotes the free energy of the mixture ( $A^{(\alpha)}$  and  $A^{(\beta)}$  are the total areas of the two phases,  $f^{(\alpha)}$  and  $f^{(\beta)}$  their free energy densities).  $F_l$  is the energy of the phase boundaries, defined as:

$$F_l = \sigma \int_{\partial\alpha} dl, \quad (3)$$

where  $\partial\alpha$  is the phase boundary.

Supposing to have  $N$  domains of the phase  $\alpha$  in a continuous phase  $\beta$ , the bending energies  $F_b$  and  $F_G$  can be written as

$$F_b = \frac{\kappa^{(\alpha)}}{2} \sum_{i=1}^N \int_{\alpha_i} dA \left( C_1 + C_2 - C_0^{(\alpha)} \right)^2 + \frac{\kappa^{(\beta)}}{2} \int_{\beta} dA \left( C_1 + C_2 - C_0^{(\beta)} \right)^2, \quad (4)$$

and

$$F_G = \kappa_G^{(\alpha)} \sum_{i=1}^N \int_{\alpha_i} dA C_1 C_2 + \kappa_G^{(\beta)} \int_{\beta} dA C_1 C_2. \quad (5)$$

Here  $(1/2)(C_1 + C_2)$  and  $C_1 C_2$  are local quantities, and denote respectively the mean and gaussian curvature of the lipid bilayer (Jülicher and Lipowsky, 1996). The bending moduli ( $\kappa^{(\alpha)}$ ,  $\kappa^{(\beta)}$ ,  $\kappa_G^{(\alpha)}$ , and  $\kappa_G^{(\beta)}$ ) and the spontaneous curvatures ( $C_0^\alpha$  and  $C_0^\beta$ ) are constants,

since the membrane is taken to be homogeneous within each domain (Jülicher and Lipowsky, 1996). Eqs. (1)–(5) do not take into account the coupling between monolayers, which would be important if the flip-flop between the two monolayer were strongly suppressed. However, for phospholipid–cholesterol mixtures, this coupling should not be relevant, because of the high flip-flop rate of cholesterol molecules (Jülicher and Lipowsky, 1996).

### 2.4. Inducing curvature on ternary membranes

The difference in bending moduli of the two phases ( $L_o$  and  $L_d$ ) causes an immediate consequence: Local bending of a liquid–liquid phase-separated bilayer carries an energy toll that is lower if the  $L_d$  phase is curved. Therefore one may expect that a ternary membrane subject to external bend constraints, exploring configuration space through the diffusion of lipid molecules and domains, would minimise its free energy by having  $L_o$  domains placed on flat (or less curved) areas, and  $L_d$  domains on the most curved ones. This effect has been described in Baumgart et al. (2003), where phase-separated GUVs were observed in different conditions, exploring at high resolution the local curvature near the domain boundaries. Many groups also investigated the coupling of composition and curvature, using various techniques to induce a local curvature in the lipid bilayer. In Parthasarathy et al. (2006) and Subramaniam (2010), for example, the curvature-induced sorting of lipids was inspected using a double bilayer system. This method consists in the deposition via vesicle rupture of a first supported lipid bilayer of uniform composition on a micro-patterned surface, followed by another deposition, again via vesicle rupture, of the DPPC/DOPC/Cholesterol bilayer of interest. The vesicle rupture method ensures a thorough mixing of the lipids, that partition again in the two phases once the bilayer is formed. Both these papers confirm the presence of  $L_d$  domains in correspondence of the high-curvature features, whereas the  $L_o$  phase prefers flat areas.

## 3. Materials and experimental methods

### 3.1. Hemispherical topography in PDMS substrates

The term “soft lithography” refers to a family of techniques for fabricating or replicating structures using soft, elastomeric elements in pattern formation (Rogers and Nuzzo, 2005). Soft lithography on poly(dimethylsiloxane) (PDMS) is used in this work to prepare a substrate with micron sized features. Poly(dimethylsiloxane) (PDMS) is a silicon-based organic polymer; after curing it is solid, elastic, and optically clear. The silicone used in this work was Sylgard® 184 by Dow Corning, which is a standard in soft lithography. PDMS is broadly used in soft lithography because it is easy and fast to work with, and ensures nanoscale precision in moulded replicas (Xia and Whitesides, 1998).

The protocol used to prepare the PDMS surface, to make a substrate capable of supporting a bilayer as shown schematically in Fig. 1(b), consists of two parts. The first part, illustrated in the steps (a)–(e) of Fig. 2, ends with the production of a PDMS master; the procedure in Subramaniam (2010) was followed, with small variations. This part of the protocol was also inspired by the soft lithography techniques described in Paunov (2003). In the second part, shown in Fig. 2(f and g), the PDMS is double casted, followed Gitlin et al. (2009).

Firstly, 2  $\mu\text{m}$  diameter Sulphate-modified Polystyrene (PS) microspheres from Invitrogen (supplied 8.1% solid volume) were diluted 1:10 with ultra-pure water. The suspension was then washed three times in ultra-pure water by centrifugation and resuspension. Aliquots were then diluted further with ultra-pure water and isopropanol (in a 2:4:4 proportion).

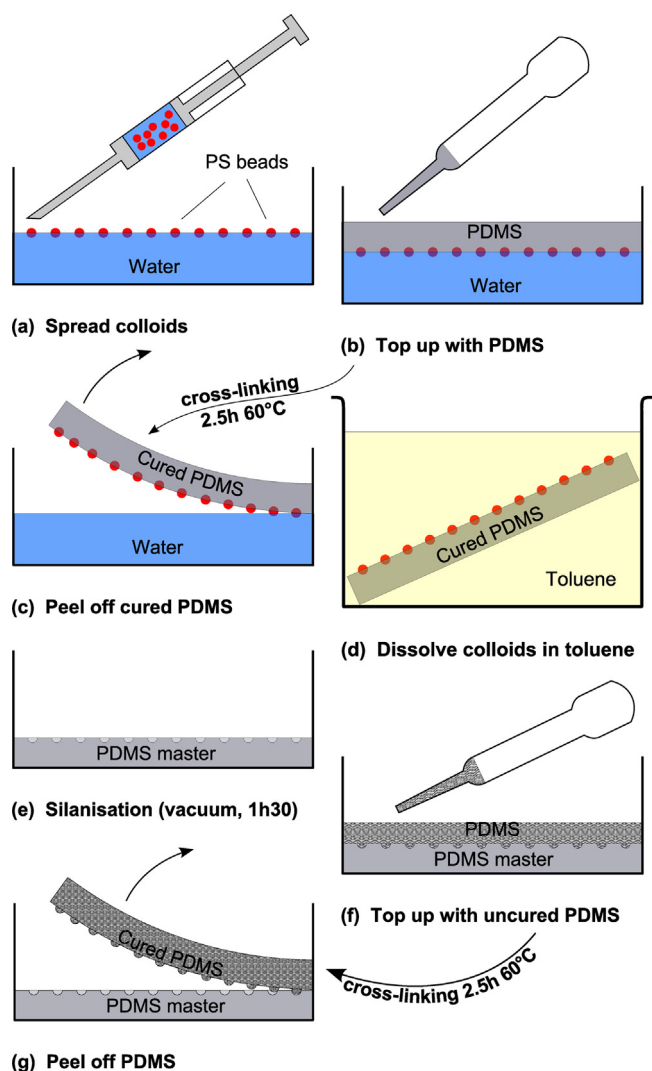


**Fig. 2.** Schematic steps in the protocol for making the master PDMS substrate with hemispherical micron-sized bumps.

The PDMS was prepared by thoroughly mixing the two components of the Sylgard® 184 kit (base and curing agent) in a 10:1 proportion in a clean plastic cup. The plastic cup was then covered with pierced parafilm and put in vacuum for half an hour, in order to degas the PDMS (the parafilm was needed to minimise contamination, e.g., by dust carried by air entering the desiccator at the end of the degassing).

A 35 mm diameter Petri dish was filled halfway to the top with ultra-pure water (18.2 M $\Omega$  cm resistivity). Next, the colloidal suspension in water and isopropanol (IPA) was spread drop-wise at the air–water interface using a 50  $\mu$ l microsyringe. A couple of minutes were waited, to allow IPA to evaporate, leaving the PS beads trapped at the air–water interface (Pieranski, 1980).

The PDMS was then carefully spread on the water surface using a disposable plastic pipette, trying to make a layer as even as possible (this is hindered by the high cohesion of the PDMS). The PDMS was then cured by placing the Petri dish in an oven at 60 °C for 2.5 h, so that the colloids became embedded in the PDMS layer.

After this curing process, the PDMS was lifted from the water surface and soaked in a beaker with toluene for 6 h, in order to dissolve the PS particles while leaving the PDMS intact. Since the PDMS swells in toluene, it was left to shrink overnight. The result of this procedure is a PDMS cylinder with a very flat surface with 1  $\mu$ m radius hemispherical holes; this is suitable to be used as a mould in the double-casting process.

The mould was placed on the bottom of an empty 35 mm Petri dish, with the patterned surface facing up, and subjected to a silanisation process. Five moulds were placed in a glass desiccator and four 40  $\mu$ l drops of 1H,1H,2H,2H-per-fluorodecyltrichlorosilane were placed on aluminium trays arranged symmetrically at the edges of the desiccator. A vacuum pump was connected to the desiccator and left running for 2 min, after which the valve of the desiccator was closed. The moulds were kept under vacuum in this silane atmosphere for 1.5 h before being removed from the desiccator. The silanisation is necessary to achieve a non-adhesive PDMS surface (Gitlin et al., 2009).

Next, uncured PDMS was cast on the silanised mould, and cured at 60 °C for 2.5 h. The new PDMS layer was then peeled away from the mould, obtaining a negative replica of the mould, i.e., a flat surface with hemispherical 1  $\mu$ m radius features (“bumps”).

While the procedure could have been stopped right after the first step in order to obtain micrometric features on the surface,

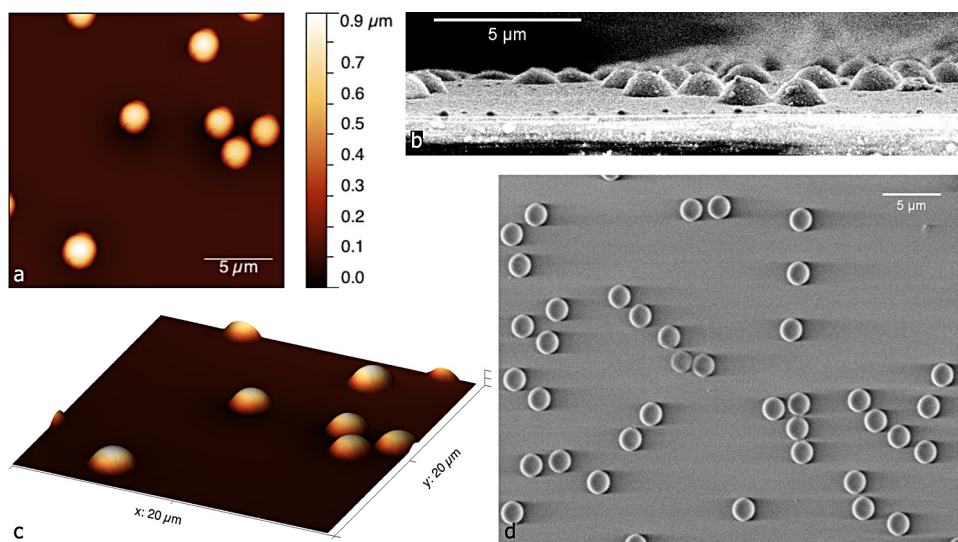


**Fig. 3.** Morphological characterisation of the PDMS substrate performed by AFM (a and c) and SEM (b and d) microscopies. (a) Shows an AFM scan, taken in non-contact mode, over an area of 25  $\times$  25  $\mu$ m<sup>2</sup> while (c) is the 3D rendering of the same area. SEM image in (b) is measured on a freshly cut, graphitised sample, positioned with the patterned surface almost vertical.

the double-casting technique was employed to avoid any chemical inhomogeneity of the patterned surface.

### 3.2. Surface characterisation

The preparation process of the patterned surface was monitored with different techniques. The proper spreading of the colloids at the air–water interface was checked by low magnification optical microscopy.

Two different scanning microscopy techniques are then used to characterise the final PDMS patterned surface: Scanning Electron Microscopy (SEM) and Atomic Force Microscopy (AFM). These techniques have been chosen because together they provide a complete morphological characterisation: AFM is very accurate in the vertical direction, but its resolution in the horizontal plane is limited by convolution effects arising from the pyramidal shape of the probe employed. In case of micron-sized objects, this might result in a wider appearance of protruding objects. This effect can be estimated, and partly corrected, by mathematical deconvolution procedures, once the shape of the probe is accurately determined.

On the other hand Scanning Electron Microscopy offers very resolved plan views of the samples, but estimates of height with this technique are always indirect and subject to possible artefacts (e.g., freeze-fracture shadow-casting combined with cryo-SEM imaging, see [Isa et al. \(2011\)](#)).

The combination of the two techniques allowed to assess accurately both the height and the lateral dimensions of the features of the PDMS surface.

AFM measurements were done either with a XE-100 microscope (Park Systems) operated in non-contact mode, using a Si probe (910M-NCHR, working at 317 kHz) and a large area scanner, or with a NanoWizard II (JPK Instruments AG) operated in contact mode with a Silicon Nitride probe (PNP-TR-20 from Nano World).

The morphology of the patterned PDMS surface, and the diameter of the protruding features, was measured by SEM imaging after graphitization of the sample surface to enhance its electrical conductivity. Images were taken with a Supra<sup>TM</sup> 40 by Zeiss, equipped with InLens detector, and operated with a beam defined by a small (7.5  $\mu\text{m}$ ) aperture and final energy of 2 keV.

The measured height of the bumps was  $0.74 \pm 0.02 \mu\text{m}$ , while the diameter was  $1.78 \pm 0.01 \mu\text{m}$ , see [Fig. 3](#). This, together with the value obtained for the height of PS colloids from the PDMS surface ( $1.1 \pm 0.02 \mu\text{m}$ ), seems to suggest that the colloids employed were actually slightly smaller (0.9  $\mu\text{m}$  in radius) than their nominal value.

### 3.3. Ternary lipid mixture

In this work Giant Unilamellar Vesicles (GUVs, defined as ranging from 5  $\mu\text{m}$  to 200  $\mu\text{m}$  in radius) were studied. The analysis actually focused only on GUVs with diameter larger than 55  $\mu\text{m}$  and smaller than 120  $\mu\text{m}$  (the upper limit being a physical constraint due to the size of the imaging chamber). A mixture of diPhyPC (1,2-diphytanoyl-sn-glycero-3-phosphocholine), DPPC (1,2-dipalmitoyl-sn-glycero-3-phosphocholine) and dihydro-cholesterol (dChol, also known as cholestanol) in chloroform was used. The phospholipids were supplied by Avanti Polar Lipids (Alabaster, AL), while the cholestanol was from Sigma. DPPC is the high  $T_m$  component in the mixture (41 °C) ([Silvius, 1982](#)), while diPhyPC has a very low  $T_m$  (<–120 °C) ([Lindsey et al., 1979](#)).

This particular lipid mixture was chosen because it optimised for imaging ([Veatch et al., 2006](#)). It is very similar to the diPhyPC/DPPC/cholesterol mixture recently used in [Veatch et al. \(2006\)](#), [Yoon et al. \(2010\)](#), [Honerkamp-Smith et al.](#)

(2008), [Honerkamp-Smith et al. \(2009\)](#). Both mixtures present liquid–liquid phase separation for a wide range of lipid composition, and both employ only saturated phospholipids. This reduces photooxidation, which is known to alter the physical properties of the bilayer ([Veatch et al., 2006](#); [Ayuyan and Cohen, 2006](#)). Reducing photooxidation is also the reason why cholesterol was replaced by cholestanol, its saturated version. This could cause small changes in the phase diagram from the better studied diPhyPC/DPPC/cholesterol ([Veatch et al., 2006](#)) reproduced in [Fig. 1\(a\)](#).

The diPhyPC/DPPC/cholestanol mixture yields phase-separated GUVs: in order to tell apart the two phases, 0.8% mol of Texas Red labelled DPPC (Texas Red DHPE, by Invitrogen) were added to the mixture; this partitions preferably in the  $L_d$  phase ([Veatch and Keller, 2005](#)).

DiPhyPC, DPPC and cholestanol were mixed in a proportion of 27:27:45 mol fraction (plus 0.8% mol Texas Red DHPE), aiming to produce GUVs with a similar fraction of  $L_o$  and  $L_d$  phases, and a transition temperature slightly (in the range 5–15 °C) above room temperature.

### 3.4. Electroformation protocol

The GUVs were prepared by electroformation, a standard technique that relies on the hydration of dry lipid film in an oscillating electric field. The protocol used is close to [Veatch and Keller \(2005\)](#). The ternary lipid composition was deposited on an Indium Tin Oxide (ITO) coated slide (Viontek Systems Ltd.), that had previously been cleaned by sonication in ultra-pure water and IPA. The deposition and spreading, being performed by hand, was the least reproducible part of this protocol, hence great care has been taken to replicate the procedure. Both the ITO coated slide and the lipid composition were heated to 60 °C, before a 30  $\mu\text{l}$  drop of lipid composition was deposited at the centre of the slide, and the spreading was performed with the help of a clean coverslip, in two slow strokes (from the centre to a side and back to the centre) without lifting the coverslip. If performed correctly, this ensured an even spreading of the lipid film, that resulted in a composition of the GUVs very similar to the starting mixture.

The slide was then placed in vacuum for at least an hour, to remove any solvent residue. An electroformation chamber was assembled using a 0.5 mm thick U-shaped spacer (cut from a sheet of Altec AlteSil), the lipid-coated slide, and another (clean) ITO coated slide.

This chamber was then filled with the swelling solution, a degassed and filtered (0.22  $\mu\text{m}$  filtered) glucose (from Sigma–Aldrich) solution in ultrapure water (200 mM), and sealed with parafilm. Binder clips were employed to make sure that the chamber held together.

Finally, the chamber was connected with two alligator clips to a function generator that provided a sinusoidal signal with 1 V peak-to-peak amplitude and 10 Hz frequency. The signal was applied for 1 h, during which the chamber was maintained at 60 °C to enhance the mixing of all the different lipids. This protocol produced a great number of GUVs with a broad radius distribution, typically between 10 and 100  $\mu\text{m}$ . After electroformation, the GUVs were stored in plastic Eppendorf tubes in the dark at room temperature until imaging, which was performed within 4 days.

### 3.5. Sample chamber

Prior to the imaging the GUVs were suspended again, usually in a 1:9 ratio, in a filtered and degassed sucrose (Sigma–Aldrich) solution (197 mM), chosen to match the osmolarity of the vesicle interior).

A SecureSeal™ circular spacer (from Grace Bio-Labs, 9 mm diameter, 120 μm thickness) was placed on a coverslip, and the resulting well was filled with the GUV suspension. The chamber was then sealed with the PDMS patterned surface placed on top, as schematically shown in Fig. 1(b). The coverslip used was a hydrophobic one (Trevigen), specifically chosen to prevent leaks.

The buoyancy, arising from the density mismatch between the glucose solution filling the GUVs and the sucrose solution in the outer medium, caused the vesicles to float and press against the patterned PDMS surface, creating a semi-supported bilayer. As discussed above, the lipid bilayer of the GUV follows the topography of the surface, and is therefore forced by the micrometric features to locally curve.

### 3.6. Epifluorescence microscopy

The imaging of the GUVs, labelled with Texas Red DHPE, was performed in epifluorescence: A Nikon Ti-E inverted microscope (imaging from below), equipped with a 40× dry Nikon objective (NA 0.75) was employed, the light source being a mercury lamp with a Texas Red filter (Semrock).

The image sequences were acquired using digital cameras (Ximea, either MQ013MG-E2 or MQ013RG-E2) and digitally recorded on a linux workstation running a custom video grabbing program developed in the lab.

Using the 40× dry objective the pixel size was 131.6 nm for both cameras. The frame rate was set to 20 fps, allowing an exposure time of 50 ms (actual time stamps of the frames reported 48.7 ms exposure time, and a 20.53 fps frame rate).

The focal plane was adjusted where the GUV membrane flattened against the PDMS patterned surface. Switching imaging mode, the PDMS features in contact with the GUV were imaged in bright field, a few seconds after the end of the acquisition of the epifluorescence video of the GUV. All image sequences were acquired at room temperature (23 °C).

## 4. Analysis and results

The two liquid phases  $L_d$  and  $L_o$  are characterised by different bending moduli, making it energetically favourable for a lipid bilayer with locally forced curvature to laterally organise so that  $L_d$  domains are placed in correspondence of high curvature points.

We expect domains to diffuse until they happen to be placed on a bump, which would then act as a trap confining their motion. From Fig. 1(f) it is already possible to see the effect of the bending modulus difference, since various  $L_d$  domains seem to get pinned by the PDMS bumps, not moving away from them for the entire imaging time.

### 4.1. Simple estimates of membrane bending on topographically patterned surfaces

It is possible to estimate the order of magnitude of this trapping effect from purely geometric considerations, assuming that there are no specific interactions between the silicone surface and the membrane.

We assume that the vesicle is pressed against the surface by buoyancy, and in this condition it is reasonable to assume that the membrane will follow the surface of the bump, and then be slightly lifted to smooth the transition to the flat region. This can be

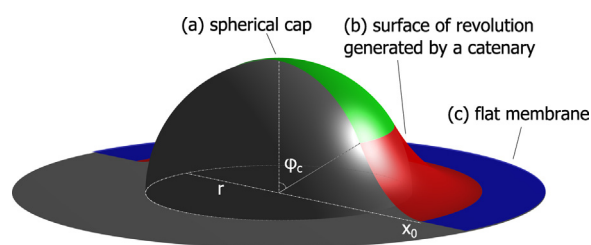


Fig. 4. Diagram of the membrane deformed by the PDMS feature (here, drawn underneath the membrane). This illustrates the situation described in the text, for which the deformation energies can be readily estimated. The membrane is approximately modelled as a spherical cap (a), stitched to a surface of revolution generated by a catenary (b), which is in turn stitched to the undeformed, flat, membrane (c).

modelled by approximating the surface in proximity to a bump as a surface of revolution. The generatrix is defined as follows:

$$z = \begin{cases} \sqrt{(r^2 - x^2)} & \text{for } 0 \leq x \leq r \cos \varphi_c \\ a \left( \cosh \left( \frac{x - x_0}{a} \right) - 1 \right) & \text{for } r \cos \varphi_c \leq x \leq x_0 \\ 0 & \text{for } x \geq x_0 \end{cases} \quad (6)$$

(see Fig. 4(a–c) respectively) where  $r$  is the radius of the bumps,  $\varphi_c$  the maximum angle from the  $z$  axis at which the membrane is still “touching” the bump,  $x_0$  is the radius of deformation (defined as the furthest distance from the centre of the bump at which the membrane is still not flat) and  $a$  is a scaling parameter for the catenary. Only one parameter is free if the generatrix is imposed to be continuous and differentiable at the junctions. The analytical expression thus obtained to model the deformed membrane then allows us to calculate the bending energy using Eqs. (4) and (5) for different values of the radius of deformation. Experimental values for the bending moduli of the two phases have been measured in Yoon et al. (2010), for a very similar system, and are  $\sim 100 k_B T$  and  $\sim 45 k_B T$  for the  $L_o$  and  $L_d$  phases respectively. Then, in reasonable conditions, the bending energies associated with the deformation induced by the bump are  $\sim 700 k_B T$  for  $L_o$  and  $\sim 300 k_B T$  for  $L_d$  while the optimal radius of deformation is  $\sim 2.6 \mu\text{m}$ .

These estimates yield two interesting consequences. First, the energy toll required for bending the membrane is two orders of magnitude smaller than the gravitational potential energy of the vesicle (which can be evaluated as  $(4/3)\pi R^3 \Delta \rho g r \approx 2.4 \times 10^{-16} \text{ J} \approx 6 \times 10^4 k_B T$ , where  $R$  is the radius of the vesicle, roughly  $60 \mu\text{m}$ , and  $\Delta \rho$  the density mismatch between the solution that fills the vesicle and the outer medium) floating at  $1 \mu\text{m}$  (which is the radius  $r$  of the topographical features) from the silicone surface. Therefore there is no doubt that the membrane will bend in proximity of the high-curvature features.

Second, there is an important energy gain ( $\sim 400 k_B T$ ) for a membrane having the  $L_d$  phase deformed in lieu of the  $L_o$  one, although the value obtained with this calculation may be overestimated for small domains: For  $L_d$  domains with a smaller radius than the one employed in the calculations, the surrounding  $L_o$  phase is likely to be at least slightly bent, therefore increasing the bending energy.

To test this in greater detail, various measurements are carried out.

### 4.2. Feature location and mean square displacement

The first step in data analysis are the segmentation and tracking of the  $L_d$  domains in the continuous  $L_o$  phase, illustrated in Fig. 1(c–f). The  $L_d$  domains are brighter than the  $L_o$  phase, so similarly to previous work (Cicuta et al., 2007), each 16 bit greyscale frame is treated with a 2D bandpass (a difference of gaussians) filter, and thresholded in order to obtain a binary image, see Fig. 1(d).

Connected white regions are identified as  $L_d$  domains provided they are sufficiently circular and with a surface area between 40 and 3000 pixel<sup>2</sup> ( $\sim 0.7\text{--}52\ \mu\text{m}^2$ ). The lower limit rejects any noise that survived the bandpass filter and the upper limit is set to avoid tracking small vesicles which sometimes appear inside the observed GUV. Image and data analysis, when not stated otherwise, are carried out using MatLab code developed ad-hoc.

The positions of the domains are determined from their centre-of-mass, and the diameters from the average between short and long axis of the approximating ellipse. To connect up positions into tracks, the positions of the domains in consecutive frames are compared and each domain is matched with the nearest feature in the previous image; if no preexisting trajectories are found close to a domain this is considered as a new track. The control on the eccentricity of domains automatically discriminates coalescing domains: when two domains unite, their individual trajectories end, and when the resulting domain equilibrates in a round shape a new trajectory begins. In the current video analysis code, we manually delete objects that are outside the GUV.

The bumps on the PDMS surface are located by processing, with a peak-finding function, the bright field image, see Fig. 1(f) taken at the end of the epifluorescence imaging. This establishes the local maxima positions with a sub-pixel precision.

The domain dynamics is investigated through the analysis of the Mean Square Displacement ( $MSD$ ) of each  $L_d$  domain. In order to assess the influence from the PDMS features, each trajectory is split in several short “sub-trajectories”, each 20 frames ( $\sim 1\text{ s}$ ) long. These sub-trajectories are long enough to measure an accurate  $MSD(\tau)$ . Dividing tracks is essential for the analysis: For example, let us assume that a  $L_d$  domain diffuses freely for half the imaging time, and then places itself on a bump. The simple calculation of its  $MSD$  from its trajectory over the entire imaging time would average on the two (supposedly different) behaviours, therefore making it very difficult to draw any conclusion. With this expedient, instead, the two behaviours are analysed separately. Similarly, this procedure also allows us to consider and control for many factors separately (as well as proximity to bumps, proximity to the centre of the GUV’s top, or interdomain distance, etc). Each of the subtrajectories is then compared with the location of the PDMS bumps. If the distance between the centre of the domain and the closest bump ever falls below the radius of the domain, the subtrajectory is flagged as “on a bump”, see Fig. 1(f).

The mean square displacement is calculated for the  $i$ -th subtrajectory as:

$$MSD_i(\tau) = \frac{1}{t_{tot} - \tau} \sum_{t=0}^{t_{tot}-\tau} (r_i(t + \tau) - r_i(t))^2, \quad (7)$$

where  $t_{tot}$  is the total time of each subtrajectory,  $r_i$  the array of positions,  $\tau$  the lag time. Considering a fixed lag time, the distribution of the  $MSD$  data is lognormal, and gives statistics both on different domains and on the history of the single domain.

In order to calculate the diffusion coefficients, looking at short lag times is preferable, since this part of the  $MSD$  is less affected by possible caging effects, and only the first 5 points of the  $MSD$  are fitted, having checked that here the  $MSD$  is linear with the lag time. The usual relation for Brownian motion in 2D is:

$$MSD_i(\tau) = 4D_i\tau, \quad (8)$$

and we expect this to hold even though  $D$  may be more complicated than in Cicuta et al. (2007), Saffman and Delbrück (1975), Petrov and Schwille (2008) because of the vicinity of the PDMS substrate.

Eq. (8) is employed also for the subtrajectories “on a bump”, since it is seen empirically to work well. We obtain a large number of measurements of diffusion coefficients, which are plotted as a distribution in Fig. 5(a). The striking aspect emerging from this

result is that a difference is appreciable in the motility of domains, depending if they are on bumps. We also looked at the distributions of the  $MSD(\tau)$  at different delay times, and they also show a difference in behaviour at all lag times, becoming more evident with increasing lag time. In Fig. 5(b), the average of the  $MSD$  of tracks on and off-bumps is shown, and confirms this result.

The analysis as described so far can be further refined: Firstly, the radius of the domains should be taken into account since it is known (Saffman and Delbrück, 1975; Cicuta et al., 2007) that the diffusivity of  $L_d$  domains in a  $L_o$  continuous phase depends on the radius. Secondly, while the exact shape of the GUV when pressed against the PDMS surface is unknown, and attempts made to directly assess it have been inconclusive because of lack of  $z$ -resolution, it is possible to check for any bias of the domain motility with the distance from the centre of the GUV, since this would be related to the distance of the bilayer from the solid substrate. These are variables that are convoluted with other effects in the distributions and means of Fig. 5(a and b). So before converging on a final analysis of domain caging by bumps, these two aspects are addressed.

#### 4.3. Assessment of the effect of domain size

The diffusion coefficients obtained from domain tracks on a single vesicle are shown in Fig. 5(c), as a function of the domain radius. The figure shows two interesting results: firstly, the data falls onto a  $1/r$  trend, which is consistent with the behaviour expected above the Saffman-Delbrück lengthscale (i.e., limit of large domains, or low membrane viscosity) (Cicuta et al., 2007; Saffman and Delbrück, 1975; Petrov and Schwille, 2008). The  $1/r$  trend (and also the  $\log(1/r)$  result for small Saffman-Delbrück lengthscale) were seen before in the bulk (Cicuta et al., 2007) under very similar phase morphology, temperature and compositions.

We note however that the presence of the solid wall nearby can strongly affect the viscous dissipation related to the domain translation, and the flow will resemble simple shear between the domain and the wall, dominating the dissipation. This is clearly very different to the case of a membrane surrounded by an infinite Newtonian fluid (Cicuta et al., 2007; Saffman and Delbrück, 1975). We are not aware of previous literature exploring this case, and we definitely expect a quantitative effect on  $D$  and perhaps even a change in the dependence  $D(R)$  on size for membrane inclusions close to a wall. For the purpose of this paper, we simply note the  $1/r$  trend, and we compare the mean motility of the on-bump domains to that of the off-bump domains. This highlights the second interesting feature of these data, namely a significant reduction in the motility on-bump.

#### 4.4. Assessment of the distance to the substrate

A possible increase of the distance between the membrane and the PDMS surface would result in an increase of the mean diffusivity of  $L_d$  domains, for two reasons: there would be less hydrodynamic drag with the surface, and then at some point the distance would be large enough that the domains would not be distorted by the bumps. To test for this, the GUV itself is identified in each frame (manually), and divided in 4 concentric regions: a central circle, and 3 annuli, see Fig. 6. Domain tracks are then binned depending on the region they are in, and the mean diffusivity of domains for each region is calculated. We determined that the motility is constant up to approximately 3/4 of the bilayer patch that appears in focus, and increases beyond that; hence all those domains that are outside the central three regions of Fig. 6 are excluded from the  $MSD$  analysis; it seems correct to consider the central regions are homogeneously “in contact” with the PDMS bumpy surface.

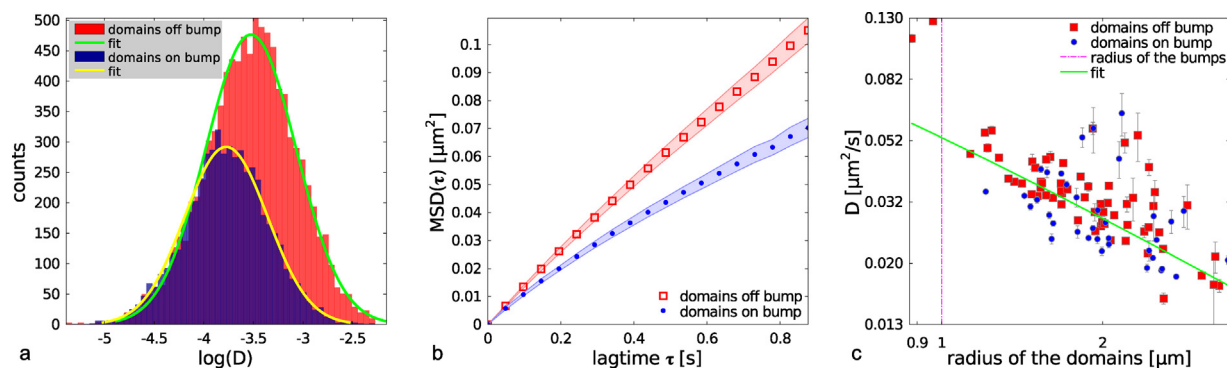


**Fig. 5.** Bumps reduce the motility of domains significantly. (a) The distribution of the natural logarithm of the diffusion coefficient  $D$  (as elsewhere in this paper, in units of  $\mu\text{m}^2/\text{s}$ ), calculated as in Eq. (8), for both subtrajectories “on bump” and “off bump”. Each distribution is shown to be well fitted by a Gaussian curve (with respectively  $\mu_{\text{on bump}} = -3.77$ ,  $\sigma_{\text{on bump}} = 0.42$ , and  $\mu_{\text{off bump}} = -3.52$ ,  $\sigma_{\text{off bump}} = 0.46$ ), meaning that the diffusion coefficient follows a lognormal distribution, with mean and standard deviation of respectively  $0.025 \pm 0.01 \mu\text{m}^2/\text{s}$  for domains “on bump”, and  $0.033 \pm 0.016 \mu\text{m}^2/\text{s}$  for domains “off bump”. (b) Shows the average over all domains of a vesicle of  $MSD(\tau)$  curves for both trajectories “on bump” or “off bump”, which also highlight obvious differences. Shading illustrates the standard error of the mean. (c) The diffusion coefficient of each domain is plotted as a function of its radius; the dependence of radius follows a  $1/r$  dependence (solid line is the best fit for this  $r$ -dependence, for “off-bump” domains). Domains on bumps have in most cases a lower diffusion coefficient.

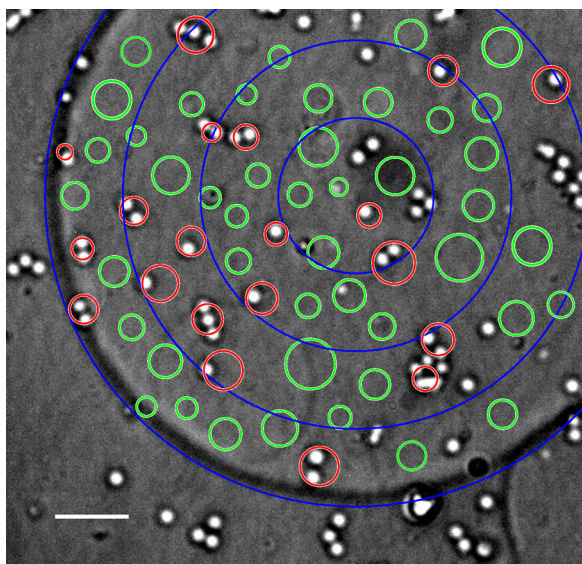


**Fig. 6.** Testing the effect of domain distance from the centre of the GUV. A bright field frame extracted from the analysis explained in Section 4.4, on which the largest blue ring outlines the GUV, while the inner ones delimit the different annuli in which the GUV is divided. Domains are here superposed as smaller circles, drawn using the positions and the radii as detected by the tracking software. Both the vesicle and the domains are obtained from the corresponding epifluorescence image. Domains that were on a PDMS bump are drawn in red, the others in green. In the bright field image, the bumps on the PDMS surface are clearly visible as bright white dots. Scale bar is  $10 \mu\text{m}$ . It was checked that the behaviour of domains was uniform in the three inner annuli of the imaging area. The motility was higher in the outer ring, so outer ring domains were excluded from the analysis (data in Figs. 5 and 7), as in this area the GUV is most likely not “in contact” with the PDMS substrate. (For interpretation of the references to colour in this figure legend, the reader is referred to the web version of the article.)

#### 4.5. Caging analysis

To investigate further the trapping mechanism, we observe the behaviour of  $L_d$  domains at longer lag times. A natural hypothesis is that the motion of a  $L_d$  domain placed on a PDMS bump should not be affected by it as long as the bump is far from the border of the  $L_d$ ; in this condition, the deformed region is all inside the  $L_d$  domain, and the bending energy should be independent from the actual relative position of the bump and the domain. In contrast, when the domain moves so that also the  $L_o$  phase starts to bend, the bending energy increases, thus making such movements not energetically

favourable. The (mean) time at which the effects of such a caging mechanism will become visible is intrinsically dependent on the radius of the  $L_d$  domain.

To analyse the behaviour of  $L_d$  domains at longer times, the  $MSD(\tau)$  is calculated on segments of 50 frames ( $\sim 2.5$  s), and the diffusion coefficients are calculated by the fit of the first five points of each  $MSD$  curve. By normalising each  $MSD$  curve with 4 times its diffusion coefficient, it is possible to compare curves of domains of different radius, even belonging to different vesicles. This allows us to pool together a large dataset, to explore as much as possible the deviation of the behaviour of  $L_d$  domains placed on a PDMS bump from Brownian motion. The normalised  $MSD$  curve of a domain moving of pure Brownian diffusion is a straight line with slope 1, while any domain whose motion is in any way confined will fall below that line.

To highlight the differences in the trend of the normalised curves depending on the radius of the domains, the on-bumps  $L_d$  domains are divided in 3 groups of increasing radius, and compared to the curve of the domains off-bumps.

As shown in Fig. 7(a), the difference in behaviour is evident between the  $L_d$  domains on- and off- bumps, and it becomes stronger as the domain radius decreases. The normalised  $MSD/4D$  data for small radius domains deviates early and significantly from the line of slope 1, showing that movements on long time scales are hindered by a trapping mechanism. Increasing the radius, the deviation is less and less pronounced, trending towards the behaviour of off-bumps  $L_d$  domains.

To investigate in detail this dependence on the radius, the same analysis was performed using smaller bins for the radius of the domains, i.e., averaging on less domains, but more similar in size. We introduce a parameter ( $\Delta h/h$ ) representing the reduction of the normalised  $MSD$ , at a fixed (chosen) lag time  $\bar{\tau} = 1.948$  s, defined as:

$$\left(\frac{\Delta h}{h}\right)_{\bar{\tau}} = \frac{\bar{\tau} - MSD(\bar{\tau})/4D}{\bar{\tau}}. \quad (9)$$

To gain insight into a possible physical mechanism underlying this complex behaviour we considered a very simple model, consisting of a 2D Brownian diffusor confined inside a circular area, and performed some numerical simulations. In this model, by a change of perspective, the diffusor represents the bump, as seen from the point of view of the domain. In the simulation, the Brownian diffusor moves with a fixed step  $\Delta r$ , in a random direction, every temporal step ( $\Delta t = 0.0487$  s, chosen to match the experimental framerate). The length of the steps ( $\Delta r = 0.1 \mu\text{m}$ ) was instead chosen so as to yield a reasonable diffusion coefficient. The

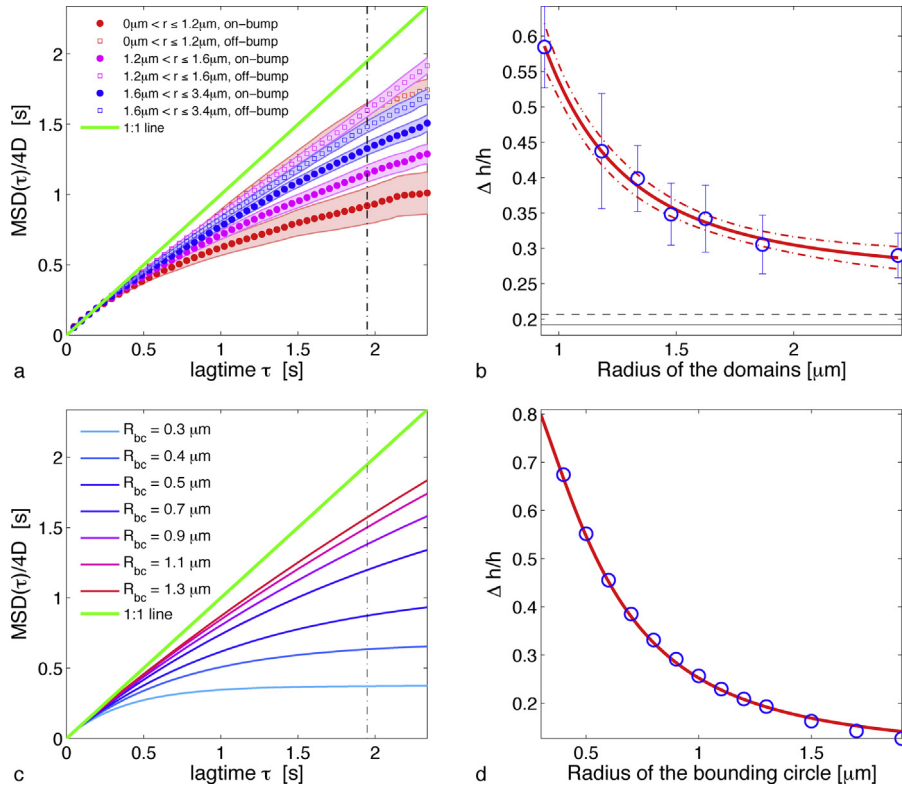


**Fig. 7.** Quantifying the caging behaviour. Experimental data in this figure pools motility data from 4 different vesicles (239 domains), and allows a more detailed analysis of the effect of bump confinement on motility of domains of varying radii. (a and b) Normalised MSD, and caging deviation parameter, from experiments. (c and d) The results of the simulations described in the text. The vertical dash-dotted black line in (a) and (c) show the value of the lagtime ( $\bar{\tau} = 1.948$  s) at which  $\Delta h/h$  was measured. In choosing  $\bar{\tau}$ , a compromise has to be made in order to appropriately show the different behaviours of the normalised curves, without being too affected by the statistical errors rising from the lack of points in the calculation of the MSD curve. In panel (b), the horizontal solid line indicates the average  $\Delta h/h$  over all the domains that are “off-bump” in panel (a), and the dashed line is the upper bound of the standard error of its mean.

confinement of the diffusor was implemented by rejecting any movement that would lead out of the bounding circle. Varying the radius of the bounding circle, we found that the normalised MSD curve is described by  $4aDR_{bc}^2(1 - e^{-4D\tau/R_{bc}^2})$ , with  $R_{bc}$  being the radius of the bounding circle, and  $a$  a phenomenological constant which depends on the step-size of the simulation.

From this function, it follows that at given lag time  $\bar{\tau}$  the reduction of normalised MSD is

$$\left(\frac{\Delta h}{h}\right)\Big|_{\bar{\tau}}(R_{bc}) = 1 - \frac{a}{4D\bar{\tau}}R_{bc}^2(1 - e^{-4D\bar{\tau}/R_{bc}^2}). \quad (10)$$

By fitting the data points from the simulation in Fig. 7(d) with Eq. 10, we find  $a = 0.907 \pm 0.003$ .

With this understanding, we turn now to the experimental data, shown in Fig. 7(b). Here too there is clearly qualitative agreement with what found in the simulations. To account well for the reduction of the normalised MSD, we include a new parameter  $c$  to take into account the finite size of the pinning bump, so that  $(\Delta h/h)$  is:

$$\left(\frac{\Delta h}{h}\right)\Big|_{\bar{\tau}}(R) = 1 - \frac{1}{4D\bar{\tau}}(R - c)^2(1 - e^{-4D\bar{\tau}/(R - c)^2}) + d, \quad (11)$$

where  $R$  is the radius of the  $L_d$  domains.  $(R - c)$  can be thought of as a reduced radius value. Notably, while  $R$  varies from domain to domain, the data fits well with  $c$  as a common value  $c = 0.39 \pm 0.08 \mu\text{m}$  which is compatible with the known size of the bumps. From this analysis, the diffusion coefficient  $D$  is also obtained by the fit:  $4D = 0.13 \pm 0.04 \mu\text{m}^2/\text{s}$ , which is compatible with the value ( $4D = 0.130 \pm 0.004 \mu\text{m}^2/\text{s}$ ) obtained from the linear fit of the MSD curves for the “on bump” domains of the same vesicle (Eq. 8). Finally,  $d$  is an offset that is most likely to be related

to the non-ideal behaviour of “off bump” domains; the fitted value is  $d = 0.26 \pm 0.01$ .<sup>1</sup>

On a side note (connected to the fact that  $d \neq 0$ ), it can be seen that even the MSD/4D curve of  $L_d$  domains not-on-bumps is slightly bent at long times. This is most likely because of membrane mediated, domain-domain interactions (Semrau et al., 2009). In vesicles with excess area,  $L_d$  domains can spontaneously have a different curvature than the surrounding  $L_o$  continuous phase, therefore budding outwards or inwards the vesicle. When such two  $L_d$  domains are close, the  $L_o$  phase is forced to bend; this mechanism acts like a repulsive force between domains, hindering their coalescence, and it is visible on vesicles with excess area and the right proportion of  $L_d$  and  $L_o$  phases (Semrau et al., 2009).

## 5. Discussion

The lateral sorting of the lipid bilayer yields  $L_d$  domains onto high-curvature portions of the surface; this is observed here in lipid vesicles, and is in agreement with experiments on Supported Lipid Bilayers (SLB) (Parthasarathy et al., 2006; Subramaniam, 2010; Ogunyankin and Longo, 2013; Yoon et al., 2006). At difference with SLBs, the vesicle system allows the membrane to drift on the surface. The observation that pinning persists against membrane drifting seems to be compatible with the high difference in energy bending when the same curvature is applied to the two phases, as estimated in Section 4.1. Another signal of the strength of the

<sup>1</sup> The fit was repeated for other choices of  $\bar{\tau}$ , yielding consistent values:  $4D = 0.16 \pm 0.07 \mu\text{m}^2/\text{s}$ ,  $c = 0.39 \pm 0.12 \mu\text{m}$ ,  $d = 0.22 \pm 0.02$  for  $\bar{\tau} = 1.461$  s, and  $4D = 0.14 \pm 0.04 \mu\text{m}^2/\text{s}$ ,  $c = 0.40 \pm 0.08 \mu\text{m}$ ,  $d = 0.23 \pm 0.02$  for  $\bar{\tau} = 1.656$  s.

pinning is the fact that the only events of “depinning” observed were caused by a  $L_d$  domain substituting another one on a bump.

The analysis of the dynamics of  $L_d$  domains is however the main result of our work here: The MSD analysis revealed, already at short timescales, an influence of the interaction between the membrane and the bumps on the motion of  $L_d$  domains.  $L_d$  domains on the bumps resulted to be less motile than domains not on a bump, being characterised by a lower value of the diffusion coefficient. However, this reduced motility seems to be a signal of a much more interesting aspect, that becomes evident when extending the MSD analysis to longer timescales. The results of the measures and the comparison with the simulations, as reported in Section 4.5, point out that a  $L_d$  domain placed on a high-curvature feature behaves qualitatively as a Brownian diffusor in a confined region, whose caging range is proportional to the radius of the domain.

If drift were absent, then it should be possible to analyse the distribution of domain position relative to the bump position, and thus explore the functional form of the pinning potential in detail. This more sophisticated analysis was considered, but ultimately not carried out because of the presence of vesicle drift which prevented an “ergodic” sampling of all domain positions inside the cage.

## 6. Conclusions

A protocol for the preparation of a chemically homogeneous, microstructured surface, was developed, based on soft lithography techniques. Its strength is that it can be modified in order to have different features structuring the surface: we worked on the micron scale so that we could deploy optical imaging, but the principle can be scaled down to controlled roughness on the scale of a few 10s of nanometers. The lower limit is set by the requirement of a sufficiently large adhesion energy of particles to the liquid–liquid interface (Pieranski, 1980).

Structuring PDMS (or in principle other soft materials) in a versatile fashion can have many applications as a substrate for lipid membrane related experiments. For example, it can be used to investigate the effects of curvature on protein localisation.

In the experiments carried out here, the microstructured surface was used to force the lipid membrane of a Giant Unilamellar Vesicle to be locally bent, in order to investigate curvature-driven sorting mechanisms in liquid–liquid phase-separated ternary membranes of DPPC/diPhyPC/Cholesterol. Dynamic analysis on  $L_d$  domains showed that it is energetically favourable for the system to place  $L_d$  domains on the high-curvature regions, as the bending energy toll due to the forced curvature of the lipid membrane is lower because of the lower bending modulus of the  $L_d$  phase in comparison to the  $L_o$  phase. Mean square displacement analysis at long timescales showed that the domains can be approximately described as Brownian diffusors confined to a circular region.

The final goal of these measurements would be a complete characterisation of the membrane shape and energy gain as a function of evolving lateral organisation; this would be an important step in the understanding of lateral organisation itself, and its role in more complex biosensor or biological systems.

## Conflict of interest

The authors declare that there are no conflict of interest.

## Acknowledgements

We acknowledge help of W. Fletcher and L. Parolini for the GUV preparation, J. Kotar for image acquisition, E. Nugent for the processing of PDMS, T. Rimoldi for help in SEM imaging, D. Orsi and J. Gallop for useful discussions. L. F. was supported by the ERASMUS exchange Programme, P. C. by EPSRC Programme Grant CAPITALS (Grant no. EPSRC EP/J017566/1) and L.C. by COST CM1101.

## References

- Ayuyan, A.G., Cohen, F.S., 2006. *Biophys. J.* 91, 2172.
- Baumgart, T., Hess, S.T., Webb, W.W., 2003. *Nature* 425, 821.
- Borsali, R., Pecora, R., 2008. *Soft-Matter Characterization*. Springer Verlag, Berlin.
- Burns, A.R., Frankel, D.J., Buranda, T., 2005. *Biophys. J.* 89, 1081.
- Christensen, S.M., Stamou, D.G., 2010. *Sensors* 10, 11352.
- Cicuta, P., Keller, S.L., Veatch, S.L., 2007. *J. Phys. Chem. B* 111, 3328.
- Collins, M.D., Keller, S.L., 2008. *Proc. Natl. Acad. Sci. U. S. A.* 105, 124.
- Collins, M.D., 2008. *Biophys. J.* 94, L32.
- Connell, S.D., Heath, G., Olmsted, P.D., Kasil, A., 2013. *Faraday Discuss.* 161, 91.
- Edidin, M., 2001. *Trends Cell Biol.* 11, 492.
- Gallop, J.L., Walrant, A., 2013. *Proc. Natl. Acad. Sci. U. S. A.* 110, 7193.
- Gitlin, L., Schulze, P., Belder, D., 2009. *Lab Chip* 9, 3000.
- Graziani, Y., Livne, A., 1972. *J. Membr. Biol.* 7, 275.
- Hirst, L.S., Uppamoochikkal, P., Lor, C., 2011. *Liquid Cryst.* 38, 1735.
- Honerkamp-Smith, A.R., Cicuta, P., Collins, M.D., Veatch, S.L., den Nijs, M., Schick, M., Keller, S.L., 2008. *Biophys. J.* 95, 236.
- Honerkamp-Smith, A.R., Veatch, S.L., Keller, S.L., 2009. *Biochim. Biophys. Acta Biomembr.* 1788, 53.
- Idema, T., Semrau, S., Storm, C., Schmidt, T., 2010. *Phys. Rev. Lett.* 104, 198102.
- Isa, L., Lucas, F., Wepf, R., Reimhult, E., 2011. *Nat. Commun.* 2, 438.
- Jülicher, F., Lipowsky, R., 1996. *Phys. Rev. E* 53, 2670.
- Kamal, M.M., Mills, D., Grzybek, M., Howard, J., 2009. *Proc. Natl. Acad. Sci. U. S. A.* 106, 22245.
- Korlach, J., Schwill, P., 1999. *Proc. Natl. Acad. Sci. U. S. A.* 96, 8461.
- Lawrence, J.C., Saslow, D.E., Michael Edwardson, J., Henderson, R.M., 2003. *Biophys. J.* 84, 1827.
- Lindsey, H., Petersen, N.O., Chan, S.L., 1979. *Biochim. Biophys. Acta Biomembr.* 555, 147.
- Lipowsky, R., Dimova, R., 2003. *J. Phys.: Condens. Matter* 15, S31.
- Marrink, S.J., Risselada, H.J., Yefimov, S., Tieleman, D.P., de Vries, A.H., 2007. *J. Phys. Chem. B* 111, 7812.
- Mouritsen, O.G., 2011. *Eur. J. Lipid Sci. Technol.* 113, 1174.
- Ogunyankin, M.O., Longo, M.L., 2013. *Analyst* 138, 3719.
- Parthasarathy, R., Yu, C.-h., Groves, J.T., 2006. *Langmuir* 22, 5095.
- Paunov, V.N., 2003. *Langmuir* 19, 7970.
- Petrov, E.P., Schwill, P., 2008. *Biophys. J.* 94, L41.
- Pieranski, P., 1980. *Phys. Rev. Lett.* 45, 569.
- Rogers, J.A., Nuzzo, R.G., 2005. *Mater. Today* 8, 50.
- Saffman, P.G., Delbrück, M., 1975. *Proc. Natl. Acad. Sci. U. S. A.* 72, 3111.
- Semrau, S., Idema, T., Schmidt, T., Storm, C., 2009. *Biophys. J.* 96, 4906.
- Silvius, J.R., 1982. *Lipid-Protein Interact.* 2, 239–281.
- Simons, K., Ikonen, E., 1997. *Nature* 387, 569.
- Sorre, B., Callan-Jones, A., Manneville, J.-B., Nassoy, P., Joanny, J.-F., Prost, J., Goud, B., Bassereau, P., 2009. *Proc. Natl. Acad. Sci. U. S. A.* 106, 5622.
- Stanich, C.A., Honerkamp-Smith, A.R., Putzel, G.G., Warth, C.S., Lamprecht, A.K., Mandala, P., Mann, E., Hua, T.D., Keller, S.L., 2013. *Biophys. J.* 105, 444.
- Subramaniam, A.B., 2010. *Adv. Mater.* 22, 2142.
- Tian, A., Baumgart, T., 2009. *Biophys. J.* 96, 2676.
- van Meer, G., Voelker, D.R., Feigenson, G.W., 2008. *Nat. Rev. Mol. Cell Biol.* 9, 112.
- Veatch, S.L., Keller, S.L., 2002. *Phys. Rev. Lett.* 89, 268101.
- Veatch, S.L., Keller, S.L., 2005. *Biochim. Biophys. Acta Mol. Cell Res.* 1746, 172.
- Veatch, S.L., Gawrisch, K., Keller, S.L., 2006. *Biophys. J.* 90, 4428.
- Veatch, S.L., Cicuta, P., Sengupta, P., Honerkamp-Smith, A., Holowka, D., Baird, B., 2008. *ACS Chem. Biol.* 3, 287.
- Xia, Y., Whitesides, G.M., 1998. *Ann. Rev. Mater. Sci.* 28, 153.
- Yoon, T.-Y., Jeong, C., Lee, S.-W., Kim, J.H., Choi, M.C., Kim, S.-J., Kim, M.W., Lee, S.-D., 2006. *Nat. Mater.* 5, 281.
- Yoon, Y.Z., Hale, J.P., Petrov, P.G., Cicuta, P., 2010. *J. Phys.: Condens. Matter* 22, 062101.